3D Printed Porous Contactors for Enhanced Oil Droplet Coalescence

Abouther Al-Shimmery,[1] Saeed Mazinani,[1] Joseph Flynn,[2] John Chew[1] and Davide Mattia[1]*

[1]Department of Chemical Engineering and Centre for Advanced Separations Engineering, University of Bath, UK and

[2]Department of Mechanical Engineering, University of Bath, UK

Corresponding author: d.mattia@bath.ac.uk

Abstract

The fabrication of 3D printed porous contactors based on triply periodic minimal surfaces (TPMS) is reported here for the first time. The structures, based on the Schwarz-P and Gyroid TPMS, were tested for oil-in-water demulsification via oil droplet coalescence and compared to a contactor with cylindrical pores and natural separation. The contactors were characterized in terms of intrinsic permeability, resistance and oil separation efficiency, for different oil concentrations (0.3, 0.4, 0.5 vol.%) in the oil-in-water emulsion, vacuum pressures (10 and 20 mbar) and thickness of the contactors (4.68 and 9.36 mm). Results show that while the Gyroid contactor has the highest resistance and lowest intrinsic permeability of all three structures, it has 18 % and 5 % higher separation efficiency than the cylindrical and Schwarz-P structures, respectively. These characteristics reflect the higher tortuosity and surface area of the Gyroid structure compared to the other two. At 90%, the Gyroid structure also has a 22% higher separation efficiency and a two order of magnitude higher separation rate for the permeate compared to natural coalescence, attributed to an 8-fold increase in oil droplet diameter of the permeate compared to the feed, as a result of passage through the contactor. Higher vacuum pressure and higher contactor thickness further increase the separation efficiency of all structures, but the effect is more pronounced for the Gyroid structure due to its higher tortuosity. These results show that 3D printing is an effective tool for the design of porous contactors where a high surface area of interaction is key to their success, paving their way to extended use in a variety of industrial applications.

keywords: 3D printing; oil-in-water demulsification; contactors; contactors

1. Introduction

The production of crude oil requires the use of large volumes of water, with approximately 8 barrels of produced water for every barrel of crude oil [1]. Environmental regulations mandate the recovery of the oil from the produced water before the latter can be discharged. However, this can be costly as produced water contains varying amounts of oil (100 – 5000 mg/L) in the form of floating layers [2] or emulsions, both unstable and stable [3]. While the first type can be easily recovered by gravity separation, stable emulsions require further energy inputs to break-up [4]. Conventional processes for oil recovery from produced water include gas flotation [5], use of chemical demulsifiers [6], American petroleum institute (API) skimmers [7], and electrostatic processes [8]. However, all of these processes generate secondary waste streams which require treatment before discharge and also present potential environmental pollution risks that must be prevented [9], thus increasing operational costs. Furthermore, the ability of these processes to effectively separate stable emulsions from produced water is somewhat limited [3]. Membrane-based processes, on the other hand, have shown significant potential in recovering oil from produced water with relatively low operational costs [10]. Membrane-based processes for oil-in-water separation can be broadly divided based on two operating principles: phase rejection [11] and oil coalescence [12]. In the former, oil is generally retained by the membrane and water passes through, whereas in the latter both oil and water pass through the membrane. The membrane acts as a high surface area contactor, favouring the coalescence of oil droplets into progressively larger ones [13] which can then be recovered by gravity separation [14]. Membrane processes based on phase rejection are fast and have high oil recovery (> 99%) but suffer from rapid flux decline due to fouling, requiring periodic cleaning to recover the initial intrinsic permeability [15, 16]. On the other hand, coalescence-based processes are less prone to fouling due to the larger pore size used, thereby requiring significantly less energy. The effectiveness of a membrane as coalescence-accelerating medium, i.e. as a contactor, is determined by its surface morphology, wettability and material thickness [17], with preference given to membrane morphologies having high pore tortuosity and high internal surface area [18]. The latter characteristics increase the collision frequency between the oil droplets and the oil droplet-interface, which, in turn, increase droplet coalescence [19].

Numerical simulations of oil-in-water demulsification in a single symmetric pore showed that the pores of membrane contactor are easily blocked by the larger oil droplets formed on the permeate side [14]. Therefore, more effective demulsification could be achieved by using asymmetric membrane contactors with pores of similar size to the emulsion droplets on the feed side and larger pores on the permeate side. The simulations showed that the larger pores on the permeate side facilitate the detachment of the larger oil droplets formed during passage through the contactor. On the other hand, by decreasing the average membrane pore size and increasing tortuosity, the internal surface area of the membrane contactors increases, which can also lead to enhanced coalescence [20]. Simulations for oil-in-water emulsions also showed that demulsification is enhanced when the membrane contactor is well wetted by the oil, as the pore wall acts as a coalescing surface [21]. Furthermore, the coalescence performance could be improved by lower flux, as this increased the emulsions' contact time with the pore walls, as it flows through the contactor [21].

An extensive review of membrane contactors for oil-in-water and water-in-oil demulsification, reported in Table S1, shows that the ideal morphology for a membrane contactor requires large pores with an asymmetric structure, high surface area and long residence times to maximise coalescence. However, a number of these characteristics are in opposition to each other, as larger pores lower the available internal surface area compared to smaller ones, and high tortuosity and long residence times decrease the overall productivity of the process. These trade-offs can be primarily attributed to limitations of current membrane manufacturing methods which do not offer great control over all these parameters simultaneously. Many of these limitations, however, could be overcome by using additive manufacturing, or 3D printing, to fabricate complex membrane shapes, while also expanding the range of usable materials beyond those currently available [22]. So far, few examples of this concept have been reported in the literature, including the fabrication of 3D printed low-fouling ultrafiltration (UF) membranes for oil-in-water separation based on phase rejection [23]; and 3D printed polysulphone supports to prepare membranes with switchable wettability surfaces via the coating of candle soot [24]. 3D printing has also been used to fabricate spacers for reverse osmosis and UF membranes, based on triply periodic minimal surfaces (TPMS), to enhance membrane flux and antifouling properties [25]. In a subsequent paper, the same group optimised the spacers to increase mass transfer in flat sheet UF membranes for protein separation, reporting significantly higher values than those obtained using conventional spacers [26]. Triply periodic minimal surfaces, based on the Schwarz-P model, have also been used to design and fabricate polydimethylsiloxane membranes as gas – liquid contactors via 3D printing [27]. A minimal surface is defined as a surface where the mean curvature is equal to zero at any point [28]. This leads to the generation of a smooth surface without any edge nor corner [26], such as soap films [29]. Triply periodic minimal surfaces occur when the minimal surface is repeated in three dimensions, as observed in many natural systems such as the mitochondria of amoebae *Chaos carolinensis* [30].

In this work, additive manufacturing (3D printing) is used for the first time to fabricate 3D printed porous contactors for oil-in-water demulsification using two TPMS morphologies, Schwarz-P and Gyroid, and their performance compared with cylindrical pore contactors.

2. Materials and methods

2.1 Materials

Urethane acrylate oligomers (acrylonitrile butadiene styrene, *VisiJet® M3-X, 3D Systems*) and a proprietary paraffin wax (*VisiJet® S300, 3D Systems*) were used to fabricate the 3D printed contactors. After printing, the wax was removed by using the EZ Rinse - C oil cleaner. All of the 3D printing materials and wax removal agents were purchased from *3D Systems*. A ProJet 3500 HD Max printer (*3D Systems*) was used in this work. Further details of the preparation and cleaning processes can be found elsewhere [23]. Deionized water (*Millipore*) and pure sunflower oil (*Tesco*) were used to prepare the oil-in-water emulsions as feed solution with different oil concentration (0.3, 0.4 and 0.5 vol. %). Sudan Blue II (*Sigma Aldrich*) was used in the visual observation tests to determine the thickness of the accumulated oil layer.

2.2 Design of 3D printed contactors

Lattice structures are typically created by tiling of a unit cell in space. However, tiling tessellated meshes (Stereolithography (STL) files) can present significant challenges at the interfaces between unit cells. If the union of two meshes is not successful, holes may appear in the mesh. To avoid this issue, this research makes use of triply periodic minimal surfaces. Here, the lattice geometry arises naturally from an infinitely repeating, implicitly-defined equation in three-dimensional Cartesian space. The general expression for the implicitly defined surface is given in (1). This formulation implies that the surface lies between the regions of space where (1) evaluates to a negative number, and those where it evaluates to a positive number. As such, the surface is the level set of all points at which the equation evaluates to zero. Equations (2) and (3), give good approximations of the Schwarz Primitive (Schwarz-P, hereafter) and the Schoen Gyroid (Gyroid, hereafter) surfaces, respectively, which are used to create lattice structures in this study:

$$F(x, y, z) = 0 \tag{1}$$

$$F(x, y, z) = \cos(f_x x) + \cos(f_y y) + \cos(f_z z) + t = 0 \tag{2}$$

$$F(x, y, z) = \sin(f_x x)\cos(f_y y) + \sin(f_y y)\cos(f_z z) + \sin(f_z z)\cos(f_x x) + t = 0 \tag{3}$$

Equations (2) and (3) both make use of frequency terms, f_x, f_y and f_z. These adjust how often the surface repeats itself in space, which is the most convenient method for scaling the size of a single unit cell. Both equations also include a level parameter, t. This manipulates the distance field of the implicit function, moving the position of the surface by changing the level set. Manipulation of the t-parameter will alter the volume on one side of the surface (enclosed by the bounding cube) with respect to the volume on the other side (Fig. 1). The mathematically defined surfaces are of limited practical use in additive manufacturing as they are infinitely thin. To address this issue, in this work two surfaces are created, and a solid material is assigned to the volume between them, resulting in a high surface-to-volume ratio structure. The level parameter is used to create two similar surfaces, each offset from the other (Fig. 1). These two surfaces never touch and therefore do not describe a manifold volume. Hence, the final stage is to enclose the two surfaces in a containing geometry (e.g. a cuboid or cylinder). Specific values of f and t used for the Schwarz-P and Gyroid are reported in section S1. The design of porous contactors using TPMSs additionally requires equations to define the structures' volume fraction, surface area, pore size and wall thickness. Detailed information on the definition and estimation of these quantities is reported in Sections S2-5.

A cylindrical-based 3D printed contactor, with the same nominal porosity as the Schwarz-P and Gyroid ones, was fabricated using the method reported in [23].

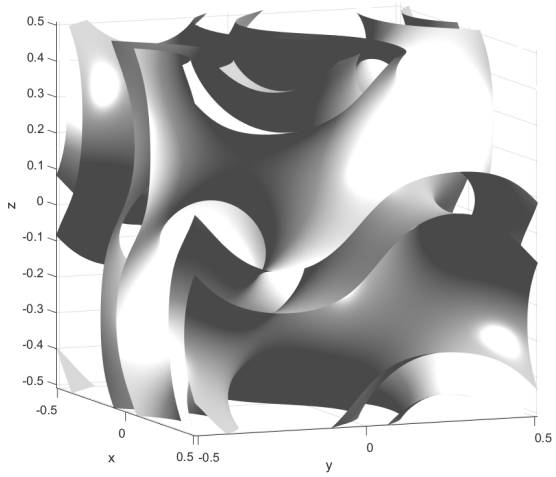

Fig. 1. Gyroid structure built using Eq. 3, with set level parameter $t = \pm 0.5$, creating a volume between the surface, thereby determining the thickness of the Gyroid's walls.

2.3 Fabrication and characterization of 3D printed contactors

The process of translating a digitally designed 3-dimensional object into a printed membrane introduces a novel set of challenges compared to traditional membrane fabrication processes: First, the more complex the object, the higher the resolution required to accurately render the object in 3D. This, in turn, leads to very large digital file sizes. For example, increasing the number of grid points needed to create the implicit surface from 150 to 800 (cfr. Fig. 2a-d), increased the file size of the Gyroid contactor from 50 Mbyte to 1.8 Gbyte. The number of grid points is a measure of the resolution of the printed object. The larger file size not only requires a longer time to transfer the file to the printer (up to 72 hrs), but ultimately might exceed the handling capacity of the printer software itself. After trial and error, a compromise resolution of 600 grid points was found to provide an adequately high resolution for the 3D printed samples and a manageable digital file.

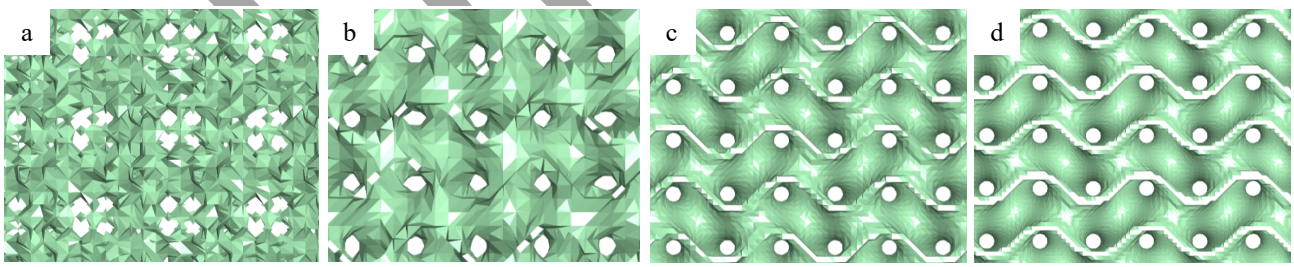

Fig. 2. STL file prepared with different resolutions for Gyroid-based 3D printed contactor (grid point values: a = 150, b = 300, c = 600, d = 800).

Furthermore, each 3D printer also has a physical resolution, with the one used in this work having a nominal resolution of 16 μm [23]. The difference between the digital model and the resulting physical objects is shown in Fig. 3. The printer produces macro- and microscopic roughness, which is quite distinct from what is obtained using traditional membrane fabrication methods [22]. It is also noted that the printer's nominal resolution relates to printing of flat surfaces; complex, non-planar surfaces are known to negatively affect it [31].

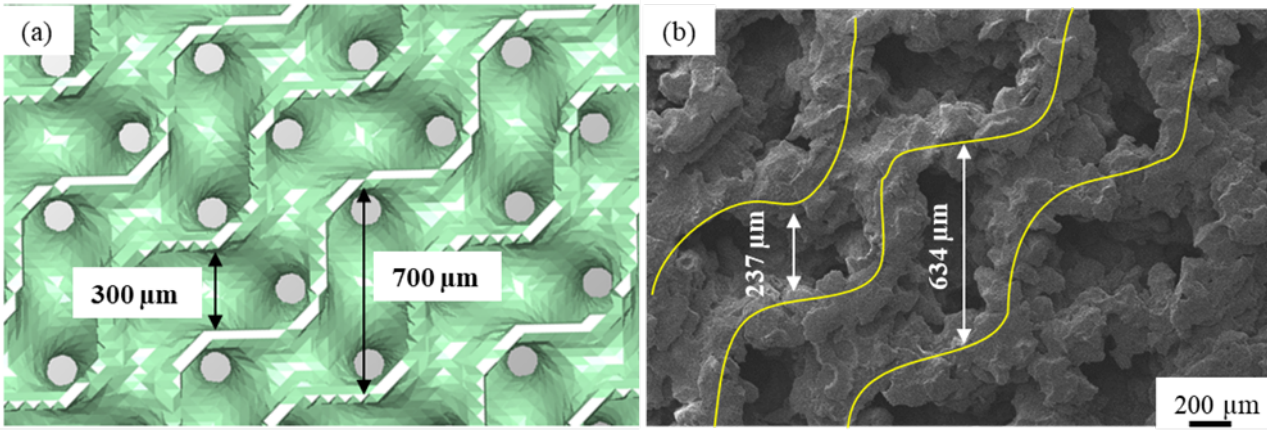

Fig. 3. Gyroid-based 3D printed contactors (a) STL digital file; (b) SEM micrograph of the 3D printed contactor (cross-section).

Further details on the printing process, wax removal from the printed membranes and their cleaning can be found in [23].

A contact angle goniometer (OCA machine, Data Physics, Germany) was used to measure the water and oil contact angles of a flat 3D printed surface at room temperature. 5 µL droplets of water and sunflower oil were used and the values reported are the average of ten measurements in different positions over the membrane surface. The surface and cross-section of the contactors was analysed via electron microscopy using a *JEOL FESEM6301F*. The surface roughness of the contactors (Ra) was determined using atomic force microscopy (AFM; Nanosurf EasyScan 2 Flex, Switzerland) under ambient conditions in the tapping mode (scan size of 5 µm, time/line of 1 s, samples/line of 256) with a monolithic silicon AFM probe (Tap190Al-G, nominal tip radius: < 10 nm).

The actual porosity of the contactors was determined by comparing the mass difference before and after was removal, i.e. with closed and open pores:

$$Mass\ change = \left(1 - \frac{M_2}{M_1}\right) \times 100 \quad (4)$$

where M_1 is the mass of contactor before wax removal (kg) and M_2 is the mass of the contactor with clean, open pores after wax removal (kg).

2.4 Preparation and characterization of emulsions

The oil-in-water emulsions were prepared by adding specific amounts of oil (0.3, 0.4, and 0.5 vol. %) in one litre of water. A homogenizer (*ULTRA-TURRAX, T 25 basic, IKA*) was used to mix the oil with water at 19,000 rpm for 5 minutes. Volume-weighted oil droplets size distributions were obtained for oil-in-water emulsions using a Malvern Mastersizer X (300 mm lens, 1.2 − 600 µm detection range, dispersion unit controller, 3000 rpm). Triplicate measurements were conducted on discrete samples and the volume median diameter D (v, 0.5) was used to compare between the oil droplet sizes in the feed and the permeate. To visualize the oil layer that had formed during the visual observation tests, a stock solution prepared by mixing sunflower oil with Sudan

Blue II with ratio 99.9:0.1 (wt. %) was used. 1 litre each of oil-in-water emulsion was prepared by mixing different amounts of (0.3, 0.4 and 0.5 vol.%) stock solution with pure water.

2.5 Contactor permeance and rejection performance

The demulsification of the oil-in-water emulsions was carried out by using a vacuum filtration setup (Fig. S4): 300 ml of oil-in-water emulsions were used in each experimental run: The first 250 ml were passed through the 3D printed contactors using vacuum filtration and collected in a separating funnel. After 1 h, 20 ml samples were taken from the bottom layer of the permeate in the separating funnel for analysis following an established procedure [12]. Three types of 3D printed contactors, Cylindrical, Schwarz–P and Gyroid, were used. Their permeance (K, LMH bar^{-1}), separation efficiency (η, %) and resistance (R_m, m^{-1}) were calculated by using the following equations:

$$K = \frac{V}{\Delta t \times A \times \Delta p} \tag{5}$$

$$\eta\,(\%) = \frac{C_F - C_P}{C_F} \tag{6}$$

$$R_m = \frac{l}{k} \tag{7}$$

where V is the volume of permeate (m^3) over time Δt (hr); A is the effective contactor surface area (m^2) (the available surface area of the contactor that the permeate can pass through); Δp is the vacuum pressure (bar); C_F is the oil concentration in the feed solution (mg/L) and C_P is the oil concentration in the permeate side (mg/L) after one hour; l is the contactor thickness (m); k is the intrinsic permeability (m^2) and was determined by using a dead-end filtration apparatus as described in [32]. Briefly, a fixed volume of water was flowed through the contactors under hydrostatic pressure. Based on Darcy's law, the rate of the filtrate flow is proportional to the hydrostatic pressure:

$$\frac{\mu u(t) l}{k} = \rho g h(t) \tag{8}$$

where μ is the dynamic viscosity of water (kg m^{-1} s^{-1}), $h(t)$ is the liquid level above the contactor which decreased with time and t is time. As the rate of filtrate flow is essentially the rate of decrease of liquid level, $u(t) = -\frac{dh}{dt}$, k can be obtained by integrating equation (8).

A turbidity meter (*EUTECH TN-100, Thermo-Scientific*) was used to determine the oil concentration in the feed and permeate [33]. The oil-in-water emulsion was initially calibrated for different known oil concentrations in terms of the intensity of scattered light in the water and read out in units of turbidity, NTU (nephelometric turbidity units). The relationship between the intensity of scattered light and the oil concentration was linear with R^2 = 0.99 (Fig. S5). The generated equation was used to measure the experimental oil concentrations. For all experiments the average of three replicate tests is reported.

2.6 Visual observation

The remaining 50 ml of the starting 300 ml emulsion were poured into a burette and a picture (using a *Canon EOS 600D*) of the top layer was taken every 30 minutes for 180 minutes to observe the increase in the thickness of the oil layer with time and quantify the separation rate of the oil phase using the 3D printed contactors and natural separation (Fig.s S9-11). *Image J* was used to measure the oil layer thickness in the recorded images.

3. Results and discussions

3.1 Structural characterization of 3D printed contactors

A summary of the structural characteristics of the Cylindrical, Schwarz-P and Gyroid 3D printed contactors is shown in Fig. 4.

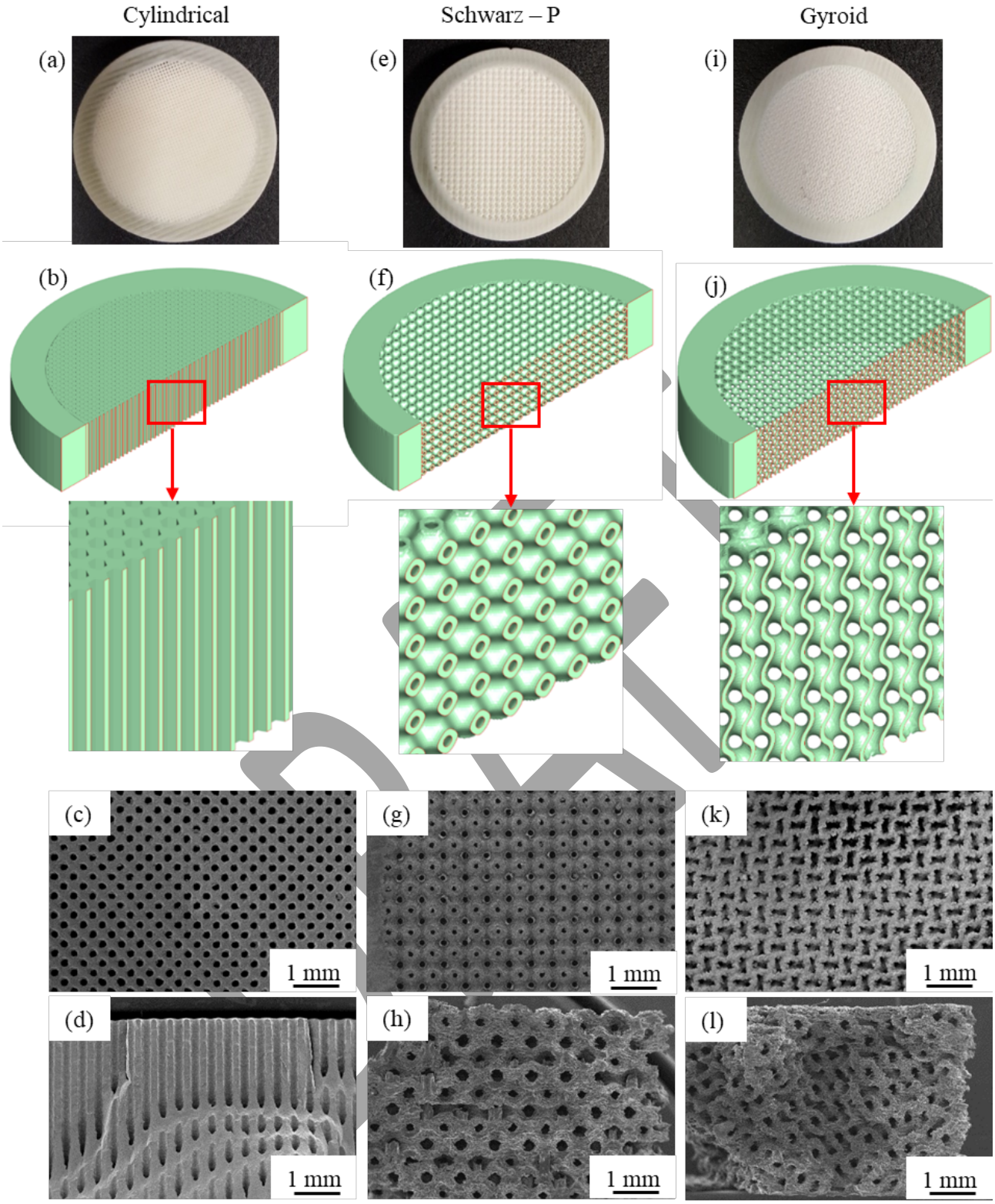

Fig. 4. Optical micrographs, CAD models, surface and cross-section SEM micrographs for Cylindrical (a, b, c, d), Schwarz-P (e, f, g, h) and Gyroid (i, j, k, l) 3D printed contactors. The diameter of all contactors is 25 mm, including a 2.5 mm rim, with a thickness of 4.68 mm or 9.36 mm.

The overall effect of the fabrication process of the 3 types of 3D printed contactors is reported in Table 1, where the theoretical pore dimension, porosity, and theoretical surface area of the porous medium were extracted from the STL files using the 3D Tool software and Autodesk Meshmixer software, respectively. The tortuosity of the Gyroid-based 3D printed contactor was taken as 1.5 from the literature [34]. The average pore sizes of the 3D printed contactors were obtained from statistical image analysis of SEM micrographs using *image J*. The pore size distribution curve of more than 100 randomly selected pores from SEM micrographs of the cylindrical-based contactors was obtained via statistical image analysis using *ImageJ* and shown in Fig. S6. Porosity was measured according to Eq. 4.

Table 1. Physical characterization of 3D printed contactors, contact angle (CA), porosity (ε), average pore diameter (D_p), roughness (R_a), tortuosity (τ) and internal surface area (SA_{int}).

	CA		ε		D_p		Ra	τ	SA_{int}
	oil	water	STL	Exper.	STL	SEM		STL	STL
	deg (± 2)			%		µm	nm	-	m^2
Cylindrical	20	83	70	54	300	225 ± 21	73 ± 2	1	7.07×10^{-3}
Schwarz-P				65	270	232 ± 14		1	8.37×10^{-3}
Gyroid				52	700	624 ± 32		1.5	11.07×10^{-3}

The flow pathway for the three structures produced is shown in Fig. 5. Although the Schwarz-P has a higher surface area than the cylindrical structure, it still has the same tortuosity, equal to 1 (Table 1). On the other hand, the Gyroid structure couples a higher surface area with a larger tortuosity [34]. As discussed in the literature, both of these factors help the coalescence process as they increase the contact time between the oil and the oleophilic surface, with the material used to print the structures being wetted more by oil than by water (Table 1).

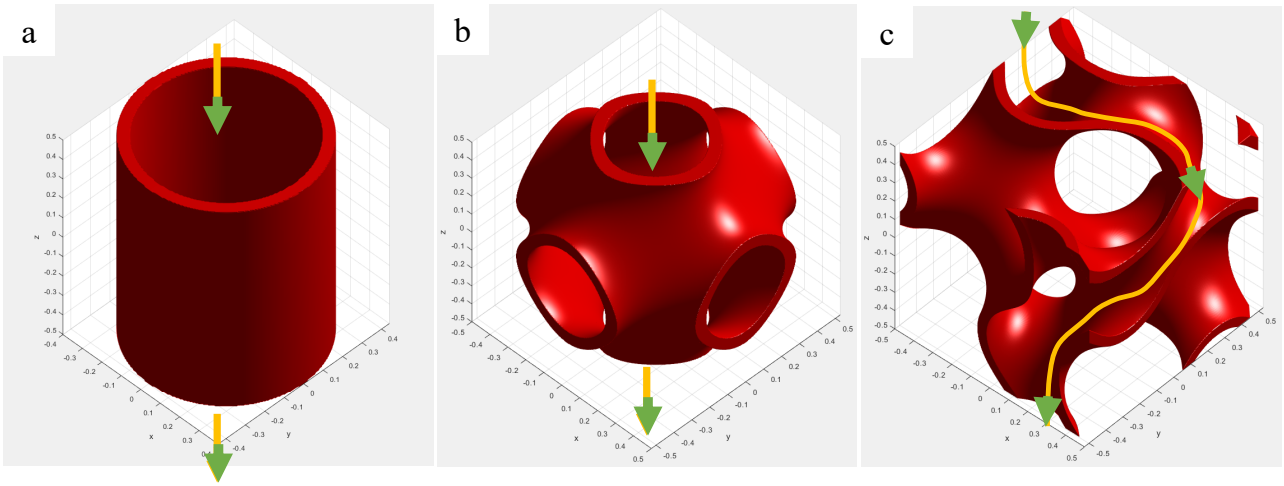

Fig 5. Liquid flow pathway through the unit cell of (a) Cylindrical (b) Schwarz-P and (c) Gyroid-based 3D printed contactors.

3.2 3D printed contactor flow characterisation

These structural differences help explain the differing performance of the structures in terms of membrane resistance, with the Gyroid structure offering a higher resistance compared to the Cylindrical and Schwarz-P ones (Table 2). This can be attributed to two factors: First, a higher tortuosity leads to higher membrane resistance [35]. Second, the triply periodic minimal surfaces generate a complex internal structure compared to the cylindrical-based 3D printed contactors, leading to an increase in the internal area facing the fluid flow (Table 1), also resulting in an increase of the fluid flow resistance through the two TPMS contactors. A higher intrinsic permeability of Schwarz-P structures compared to Gyroid ones has been observed previously [36], and attributed to the fact that the intrinsic permeability of a fluid is inversely proportional to the corresponding smallest specific surface [37].

Table 2. Intrinsic permeability (k), membrane resistance (R_m) and pure water permeance (K_w)for 3D printed contactors with thickness 4.68 mm.

	k_{exp}	k_{STL}	k_{eff}	R_m	K_w	
					10 mbar	20 mbar
	m^2			m^{-1}	LMH bar^{-1}	
Cylindrical	7.39×10^{-10}	19.7×10^{-10}	8.54×10^{-10}	6.33×10^{6}	$1.76 \pm 0.02 \times 10^{7}$	$3.61 \pm 0.20 \times 10^{7}$
Schwarz-P	1.05×10^{-10}	15.9×10^{-10}	10.9×10^{-10}	4.44×10^{7}	$4.87 \pm 0.04 \times 10^{6}$	$1.00 \pm 0.02 \times 10^{7}$
Gyroid	5.44×10^{-11}	71.4×10^{-10}	42.2×10^{-10}	8.60×10^{7}	$3.00 \pm 0.01 \times 10^{6}$	$6.00 \pm 0.05 \times 10^{6}$

*error for all intrinsic permeability measured values is in the order of 10^{-13}.

The fact that the contactors used in this work are designed with regular features, unlike traditional membranes, allows using the experimental data for the membrane resistance to estimate the effect of deviation in structural parameters (pore size, porosity, tortuosity) of the printed contactors from the digital drawing. From Darcy's law, the intrinsic permeability is:

$$k \propto \frac{\varepsilon D_p^2}{32\tau} \tag{8}$$

where the values for ε, D and τ are those defined in the digital drawing. For the cylindrical case, Eq.8 becomes an exact relation (via the Haagen-Poiseuille equation). Using the values from the digital drawing, one can calculate the theoretical intrinsic permeability (k_{STL}). With the available experimental values for the average pore size and porosity (Table 1), one can then calculate an effective intrinsic permeability, corrected for those variables that can be directly measured (k_{eff}). This corrected value can then be compared to the experimentally measured one (k_{exp}), as reported in Table 2. For the cylindrical case, the difference between the measured value and k_{eff} is small, signalling that deviations in the printed object from the digital drawing for tortuosity and internal surface area, which cannot be independently measured, are quite small. On the other hand, differences are much more significant for the Schwarz-P and the Gyroid structures (Table 2), indicating not only larger deviations between the digital drawing and the printed structures, but also the fact that the more complex geometry cannot be simply modelled using Eq. 8. This is particularly the case for the Gyroid structure,

which has a complex pore structure (Fig.5) which cannot be effectively measured solely by statistical image analysis using SEM (Table 1).

The pure water and oil-in-water emulsion permeance values for the three different 3D printed contactors (Cylindrical, Schwarz-P and Gyroid) are presented in Fig. 6. Different oil concentrations (0.3, 0.4, and 0.5 vol. %) of the oil-in-water emulsion and two vacuum pressure differences (10 and 20 mbar) were tested. The permeance doubled for all the 3D printed contactors when the initial vacuum pressure was doubled from 10 to 20 mbar, following Darcy's law (Table 2). Similarly, the permeance halved when the contactors' thickness was doubled, also in line with Darcy's law (cfr. Fig.6a and 6c). On the other hand, permeance decreased with increasing oil concentration. This is attributed to the high affinity between oil droplets and contactor material (low oil contact angle, cfr. Table 1). Such good wettability might have also led to the formation of a continuous oily layer on the inner surface of the contactors, further increasing adhesion between the oil and the contactor surface [38]. It has also been observed in the literature that an increase in thickness of the oily layer on the membrane's surface, resulting from the higher oil concentration in the feed, leads, in turn, to an increase in the overall membrane resistance against fluid flow [39].

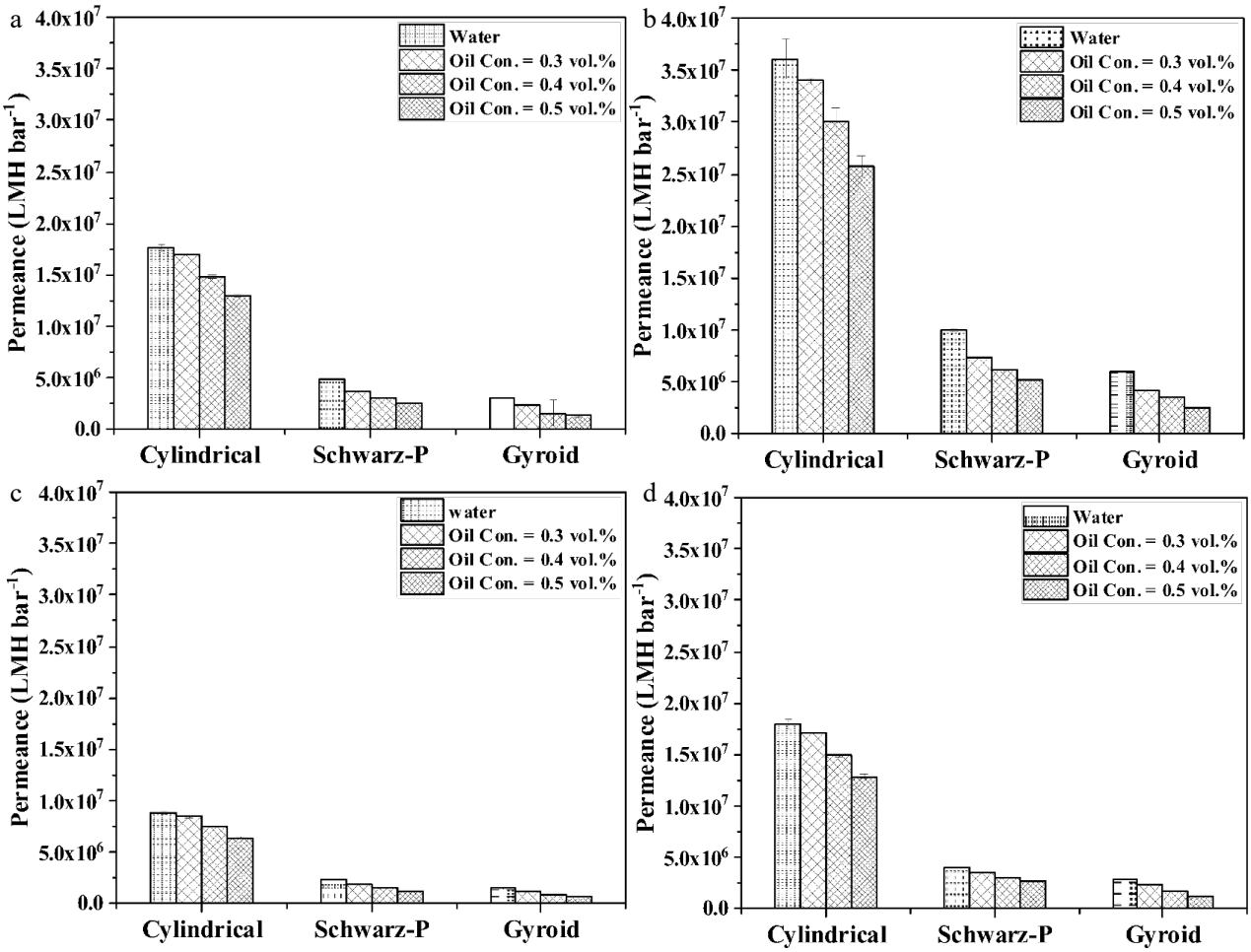

Fig. 6. Pure water and oil-in-water emulsion (0.3, 0.4 and 0.5 vol. %) permeance of the 3D printed contactors for (a) thickness = 4.68 mm, vacuum pressure = 10 mbar, (b) thickness = 4.68 mm, vacuum pressure = 20 mbar, (c) thickness = 9.36 mm, vacuum pressure = 10 mbar, and (d) thickness = 9.36 mm, vacuum pressure = 20 mbar.

3.3 3D printed contactors separation performance

The effect of varying vacuum pressure, oil concentration in the feed emulsion and the 3D printed contactors thickness on the ability of the latter's ability to separate the oil from water is shown in Fig. 8. Doubling the vacuum pressure, while doubling the permeance (cfr. Fig.s 6a and 6b) leads only to a modest decrease in oil separation (cfr. Fig.s 7a and 7b), for the three types of contactors tested. Although a higher permeance would result in a shorter residence time, thereby reducing the overall coalescence [21], the very good wetting of the contactors by the oil can explain the limited effect of doubling the vacuum pressure on the separation efficiency. It can be speculated that for a threshold higher vacuum value, the decrease in separation would be more significant, mitigating the positive influence of the good wettability [17].

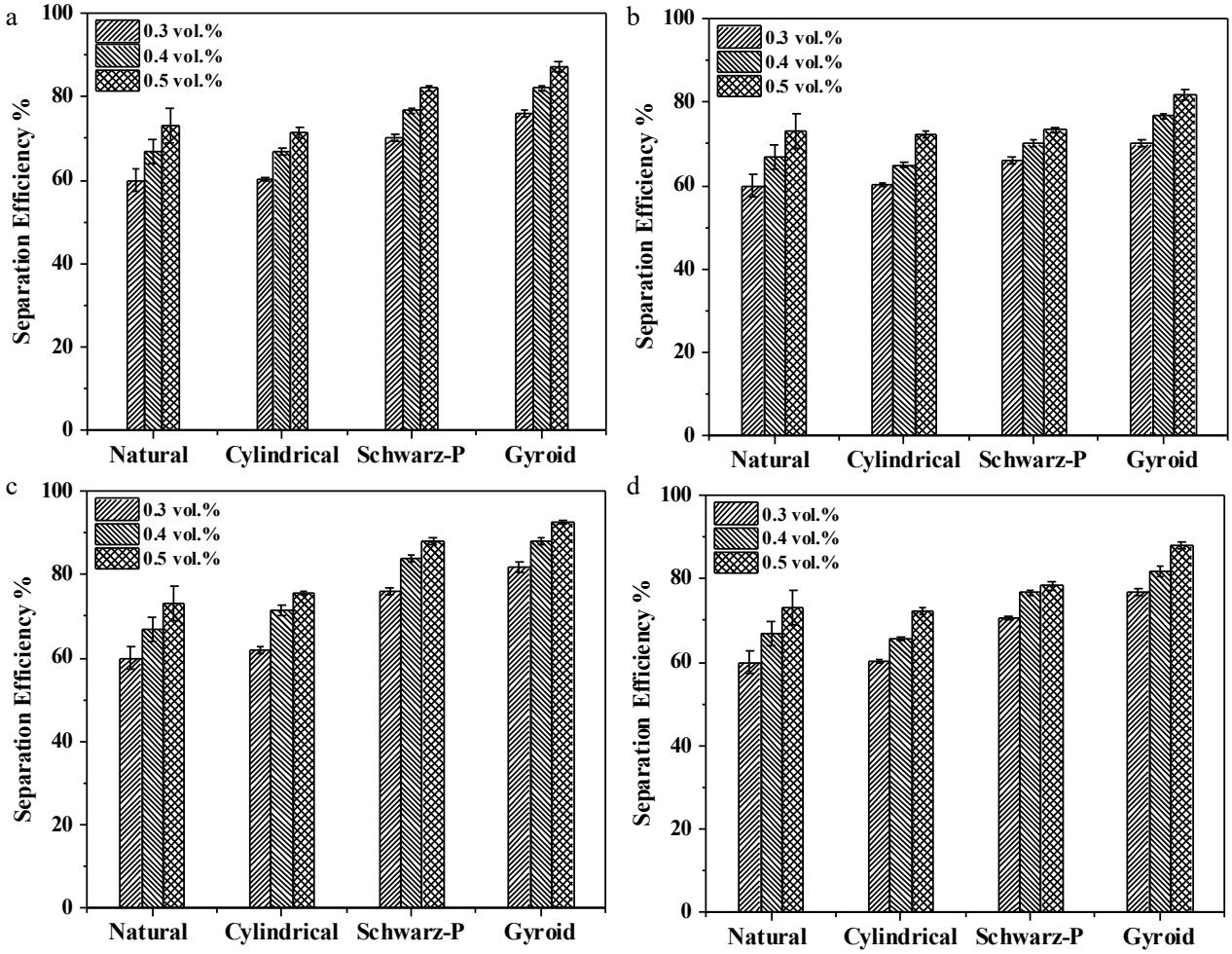

Fig. 7. Separation efficiency of natural demulsification process and of the 3D printed contactors for oil-in-water emulsions (0.3, 0.4 and 0.5 vol. %) and for (a) thickness = 4.68 mm, vacuum pressure = 10 mbar, (b) thickness = 4.68 mm, vacuum pressure = 20 mbar, (c) thickness = 9.36 mm, vacuum pressure = 10 mbar, and (d) thickness = 9.36 mm, vacuum pressure = 20 mbar.

Oil separation increased with increasing oil concentrations (0.3, 0.4, 0.5 vol. %) in the feed emulsion, for the three types of contactors tested. This can be attributed to an enhancement of the collision rate between the oil droplets [40], which gave rise to more efficient collisions between the dispersed droplets and thereby increasing the rate of coalescence. A similar trend was observed for oil-in-water emulsions and

polytetrafluoroethylene (PTFE) flat sheet membranes, albeit for significantly higher oil concentrations (from 0.5 to 5.0 vol. %) [41]. An opposite behaviour was observed for 5 vol. % isodecane-in-water emulsions, also using PTFE flat sheet membranes [42]. Finally, a doubling of the thickness of the contactor (from 4.68 to 9.36 mm), yields a further increase in oil separation (Fig.s 7c and 7d). For 10 mbar of vacuum pressure and 0.5 vol. % oil in the feed emulsion, the increase is 5, 6 and 6 % for the cylindrical, Schwarz-P and Gyroid based 3D printed contactors, respectively. This is attributed to an increase in the residence time through the contactors which allowed more opportunities for the oil droplets to come in contact and merge, as also observed via numerical simulation [21]. The increase for the Gyroid contactor over natural demulsification was of 22%, and, at around 90%, is broadly comparable with the separation efficiency of conventional membrane coalescers with smaller pores in the microfiltration range (Table S1), but with significantly lower pressure loss.

3.4 Oil coalescence

As the role of a contactor is to accelerate the separation of the two phases, a proper assessment of its performance requires observing what happens to the permeate after leaving the contactor itself. An in-depth study of the coalescence of the permeate from the Gyroid contactor was performed, as this structure provided the best results in terms of separation efficiency. A Malvern Mastersizer was first used to measure the average diameter of the oil droplets in the feed and permeate, showing an increase from D (v, 0.5) = 11 ± 1 μm in the feed to 42 ± 2 μm, 56 ± 3 μm and 85 ± 4 μm in the permeate with initial concentration of 0.3, 0.4 and 0.5 vol. %, respectively (Fig. 8). This result is further supported by optical observation of the permeate (Fig. S8).

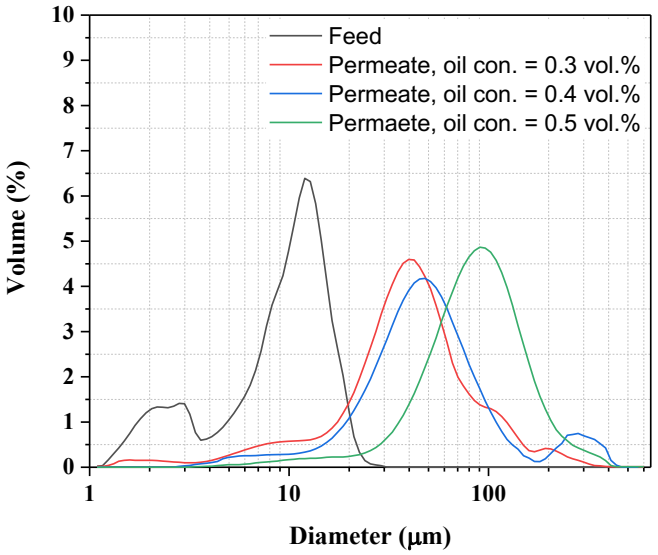

Fig. 8. Oil droplet size distribution in the oil-in-water emulsion feed and in the permeate, with different oil concentrations going through the Gyroid-based 3D printed contactors.

It is interesting to note that the average droplet size of the feed emulsion is significantly smaller than the average pore diameter of the Gyroid-based membrane (Table 1). As discussed in the introduction, the large

pores of the contactors reported here should work against oil coalescence given that they result in an overall lower surface area compared to contactors with smaller pores [41]. However, herein lies the advantage of using 3D printing which enables the fabrication of ordered, highly tortuous structures, such as the Gyroid contactor, which increases contact time without increasing the overall thickness of the contactor. This results in having the advantages of a thin membrane (low resistance) and those of one with a high surface area (high contact time).

Finally, the separation rate of the permeate from the Gyroid-based 3D printed contactors into a burette for the three initial oil concentrations versus natural oil-in-water demulsification is reported in Fig. 9, with the associated optical micrographs shown in Fig.s S9-11.

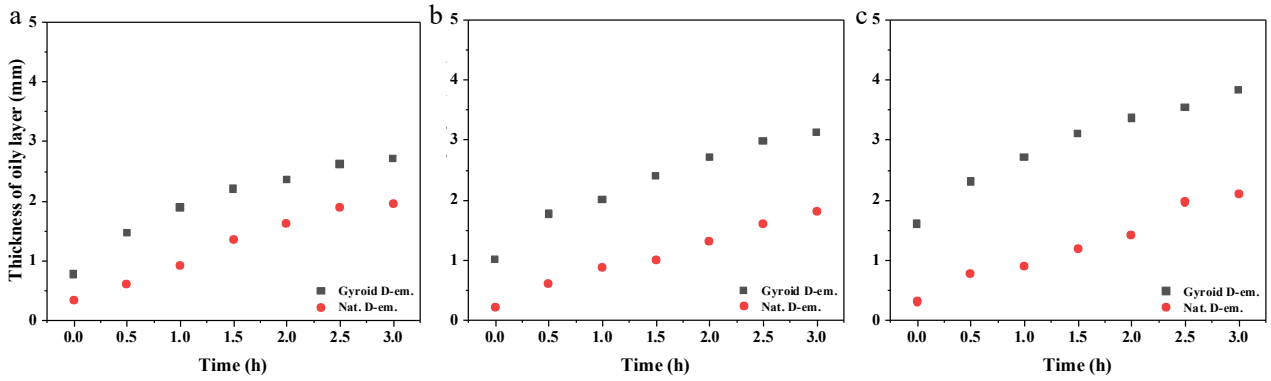

Fig. 9. Demulsification using Gyroid-based 3D printed contactor at vacuum pressure = 10 mbar with different oil concentrations (a) 0.3 vol. %, (b) 0.4 vol. % and (c) 0.5 vol. %, compared to natural demulsification.

The Gyroid clearly leads to a significant acceleration of the demulsification process, which increases with initial oil concentration. This effect is ascribed to the formation of larger oil droplets resulting from the passage into the contactor. In fact, according to Stoke's law, the velocity of an oil droplet, v, in the stationary emulsion is proportional to the square of the droplet diameter:

$$v = \frac{d^2(\rho_w - \rho_o)\, g}{18\mu} \tag{9}$$

where g is the acceleration due to the gravity, d the oil droplet diameter, μ is the water viscosity (0.00102 kg/m.s), ρ_w is the water density (1000 kg/m^3), ρ_o is the oil phase density (830 kg/m^3). An increase in the average droplet diameter D (v, 0.5) from 11 µm of the feed to 85 µm of the permeate, would result in an increase in droplet rise velocity of two orders of magnitude, from 0.11 to 6.65 × 10^{-4} m/s. This would, in turn, result in a much faster separation between the oil and the water phases, easing the oil's recovery.

4. Conclusions

In this work, a 3D printer was used to fabricate two different types of porous contactors based on triply periodic minimal surfaces (TPMS), namely Schwarz-P and Gyroid structures. The performance of these contactors was compared to both natural coalescence and a cylindrical pore contactor, also 3D printed, in terms of the efficiency of separation of oil-in-water emulsions. The effects of several design and process parameters including contactor thickness, the oil concentration in the feed and the vacuum pressure on the separation performance of the 3D printed contactors were studied, using a sunflower oil-in-water emulsion as a model system. The results showed that the 3D printed Gyroid contactor had the highest separation performance (93%) using a low vacuum pressure of 10 mbar, whereas the cylindrical structure only achieved 71% separation, similar to natural coalescence. This is attributed to the complex structure of the TPMS-based 3D printed Gyroid contactors, which provide high surface area and tortuosity. These results show that 3D printing can be an effective manufacturing technique for the fabrication of tailored porous contactors providing high surface areas and long residence times, opening the way to their use in a wide range of applications.

Acknowledgements

The work is supported by UK Engineering and Physical Sciences Research Council (EP/M01486X/1). A. A.-S. acknowledges the financial support of the Ministry of Higher Education and Scientific Research of Iraq. All data created during this research are openly available from the University of Bath data archive at: https://doi.org/10.15125/BATH-00641

References

1. Pierce, D., K. Bertrand, and C. CretiuVasiliu. *Water recycling helps with sustainability*. in *SPE Asia Pacific Oil and Gas Conference and Exhibition*. 2010. Society of Petroleum Engineers.
2. Tummons, E.N., et al., *Behavior of oil droplets at the membrane surface during crossflow microfiltration of oil–water emulsions.* Journal of Membrane Science, 2016. **500**: p. 211-224.
3. Um, M.-J., et al., *Flux enhancement with gas injection in crossflow ultrafiltration of oily wastewater.* Water research, 2001. **35**(17): p. 4095-4101.
4. Li, J. and Y. Gu, *Coalescence of oil-in-water emulsions in fibrous and granular beds.* Separation and Purification Technology, 2005. **42**(1): p. 1-13.
5. Moosai, R. and R.A. Dawe, *Gas attachment of oil droplets for gas flotation for oily wastewater cleanup.* Separation and purification technology, 2003. **33**(3): p. 303-314.
6. Mohammed, R., et al., *Dewatering of crude oil emulsions 3. Emulsion resolution by chemical means.* Colloids and Surfaces A: Physicochemical and Engineering Aspects, 1994. **83**(3): p. 261-271.
7. Veil, J., B. Langhus, and S. Belieu. *Downhole oil/water separators: An emerging produced water disposal technology*. in *SPE/EPA exploration and production environmental conference*. 1999.
8. Noïk, C., J. Chen, and C.S. Dalmazzone. *Electrostatic demulsification on crude oil: A state-of-the-art review*. in *International Oil & Gas Conference and Exhibition in China*. 2006. Society of Petroleum Engineers.
9. Maiti, S., et al., *Removal of oil from oil-in-water emulsion using a packed bed of commercial resin.* Colloids and Surfaces A: Physicochemical and Engineering Aspects, 2011. **389**(1): p. 291-298.
10. Tanudjaja, H.J., et al., *Effect of cross-flow velocity, oil concentration and salinity on the critical flux of an oil-in-water emulsion in microfiltration.* Journal of Membrane Science, 2017. **530**: p. 11-19.

11. Chakrabarty, B., A. Ghoshal, and M. Purkait, *Cross-flow ultrafiltration of stable oil-in-water emulsion using polysulfone membranes.* Chemical Engineering Journal, 2010. **165**(2): p. 447-456.
12. Hlavacek, M., *Break-up of oil-in-water emulsions induced by permeation through a microfiltration membrane.* Journal of membrane science, 1995. **102**: p. 1-7.
13. Kota, A.K., et al., *Hygro-responsive membranes for effective oil–water separation.* Nature Communications, 2012. **3**: p. 1025.
14. Mino, Y., et al., *Numerical simulation of coalescence phenomena of oil-in-water emulsions permeating through straight membrane pore.* Colloids and Surfaces A: Physicochemical and Engineering Aspects, 2016. **491**: p. 70-77.
15. Kasemset, S., et al., *Effect of polydopamine deposition conditions on fouling resistance, physical properties, and permeation properties of reverse osmosis membranes in oil/water separation.* Journal of Membrane Science, 2013. **425-426**: p. 208-216.
16. Cumming, I.W., R.G. Holdich, and I.D. Smith, *The rejection of oil by microfiltration of a stabilised kerosene/water emulsion.* Journal of Membrane Science, 2000. **169**(1): p. 147-155.
17. Li, X., et al., *Sensitivity of coalescence separation of oil–water emulsions using stainless steel felt enabled by LBL self-assembly and CVD.* RSC Advances, 2015. **5**(87): p. 71345-71354.
18. Si, Y., et al., *Superelastic and superhydrophobic nanofiber-assembled cellular aerogels for effective separation of oil/water emulsions.* ACS nano, 2015. **9**(4): p. 3791-3799.
19. Hong, A.C., A.G. Fane, and R.P. Burford, *The effects of intermittent permeate flow and crossflow on membrane coalescence of oil-in-water emulsions.* Desalination, 2002. **144**(1): p. 185-191.
20. Kawakatsu, T., et al., *Emulsion breakdown: mechanisms and development of multilayer membrane.* AIChE journal, 1999. **45**(5): p. 967-975.
21. Kagawa, Y., et al., *Permeation of concentrated oil-in-water emulsions through a membrane pore: numerical simulation using a coupled level set and the volume-of-fluid method.* Soft matter, 2014. **10**(40): p. 7985-7992.
22. Low, Z.-X., et al., *Perspective on 3D printing of separation membranes and comparison to related unconventional fabrication techniques.* Journal of Membrane Science, 2017. **523**: p. 596-613.
23. Al-Shimmery, A., et al., *3D printed composite membranes with enhanced anti-fouling behaviour.* Journal of Membrane Science, 2019. **574**: p. 76-85.
24. Yuan, S., et al., *Super-hydrophobic 3D printed polysulfone membranes with a switchable wettability by self-assembled candle soot for efficient gravity-driven oil/water separation.* Journal of Materials Chemistry A, 2017. **5**(48): p. 25401-25409.
25. Sreedhar, N., et al., *3D printed feed spacers based on triply periodic minimal surfaces for flux enhancement and biofouling mitigation in RO and UF.* Desalination, 2018. **425**: p. 12-21.
26. Sreedhar, N., et al., *Mass transfer analysis of ultrafiltration using spacers based on triply periodic minimal surfaces: Effects of spacer design, directionality and voidage.* Journal of Membrane Science, 2018. **561**: p. 89-98.
27. Femmer, T., A.J. Kuehne, and M. Wessling, *Print your own membrane: direct rapid prototyping of polydimethylsiloxane.* Lab on a Chip, 2014. **14**(15): p. 2610-2613.
28. Gandy, P.J., et al., *Nodal surface approximations to the P, G, D and I-WP triply periodic minimal surfaces.* Chemical physics letters, 2001. **336**(3): p. 187-195.
29. Lord, E.A. and A.L. Mackay, *Periodic minimal surfaces of cubic symmetry.* Current Science, 2003: p. 346-362.
30. Deng, Y. and M. Mieczkowski, *Three-dimensional periodic cubic membrane structure in the mitochondria of amoebaeChaos carolinensis.* Protoplasma, 1998. **203**(1-2): p. 16-25.
31. Nawada, S., S. Dimartino, and C. Fee, *Dispersion behavior of 3D-printed columns with homogeneous microstructures comprising differing element shapes.* Chemical Engineering Science, 2017. **164**: p. 90-98.
32. Chew, Y.J., W. Paterson, and D. Wilson, *Fluid dynamic gauging: a new tool to study deposition on porous surfaces.* Journal of Membrane Science, 2007. **296**(1-2): p. 29-41.
33. Pal, R., *Techniques for measuring the composition (oil and water content) of emulsions—a state of the art review.* Colloids and Surfaces A: Physicochemical and Engineering Aspects, 1994. **84**(2): p. 141-193.

34. Li, L., et al., *Gyroid nanoporous membranes with tunable permeability.* ACS nano, 2011. **5**(10): p. 7754-7766.
35. Lee, A., J.W. Elam, and S.B. Darling, *Membrane materials for water purification: design, development, and application.* Environmental Science: Water Research & Technology, 2016. **2**(1): p. 17-42.
36. Jung, Y. and S. Torquato, *Fluid permeabilities of triply periodic minimal surfaces.* Physical Review E, 2005. **72**(5): p. 056319.
37. Femmer, T., A.J. Kuehne, and M. Wessling, *Estimation of the structure dependent performance of 3-D rapid prototyped membranes.* Chemical Engineering Journal, 2015. **273**: p. 438-445.
38. Agarwal, S., et al., *Role of surface wettability and roughness in emulsion separation.* Separation and Purification Technology, 2013. **107**: p. 19-25.
39. Kukizaki, M. and M. Goto, *Demulsification of water-in-oil emulsions by permeation through Shirasu-porous-glass (SPG) membranes.* Journal of Membrane Science, 2008. **322**(1): p. 196-203.
40. Zolfaghari, R., et al., *Demulsification techniques of water-in-oil and oil-in-water emulsions in petroleum industry.* Separation and Purification Technology, 2016. **170**: p. 377-407.
41. Hong, A., A. Fane, and R. Burford, *Factors affecting membrane coalescence of stable oil-in-water emulsions.* Journal of membrane science, 2003. **222**(1): p. 19-39.
42. Daiminger, U., et al., *Novel techniques for iol/water separation.* Journal of membrane science, 1995. **99**(2): p. 197-203.